Supporting Information

Theoretical Analysis of Norrish Reaction Mechanism in Aliphatic Polyamide

Jingcheng Sang,[†] Yuuichi Orimoto[‡] and Yuriko Aoki[*,‡]

[†] Department of Interdisciplinary Engineering Sciences, Chemistry and Materials Science, Interdisciplinary Graduate School of Engineering Sciences, Kyushu University, 6-1 Kasuga Park, Fukuoka 816-8580, Japan

[‡] Department of Material Sciences, Faculty of Engineering Sciences, Kyushu University, 6-1 Kasuga Park, Fukuoka 816-8580, Japan

***E-mail:** aoki.yuriko.397@m.kyushu-u.ac.jp.

Table S1. Parameters of singlet vertical excitations (UV absorption) from S_0 to S_1-S_5 (S_n and T_n denote the *n*th ES in singlet and triplet) based on the S_0 geometry (Figure 1b) of methyl propyl ketone (MPK) at the default time-dependent density functional theory (TD-DFT) level (PBE0-D3/6-31G(d,p)).

Electronic excitation	**Energy (eV)**	**λ^a (nm)**	**f^b**	**Contribution (>10%)**	**Transitions[c]**	**Assignments[d]**
$S_0 \rightarrow S_1$	4.49	276	0	99.0	H → L	$^1[n \rightarrow \pi^*_{(O=C)}]$
$S_0 \rightarrow S_2$	7.94	156	0.001	34.1	H−2 → L	$^1[\pi_{(O=C)} \rightarrow \pi^*_{(O=C)}]$
				32.4	H−1 → L	$^1[n \rightarrow \pi^*_{(O=C)}]$
				29.9	H−3 → L	$^1[\pi_{(O=C)} \rightarrow \pi^*_{(O=C)}]$
$S_0 \rightarrow S_3$	7.96	156	0.001	58.0	H−1 → L	$^1[n \rightarrow \pi^*_{(O=C)}]$
				29.0	H−3 → L	$^1[\pi_{(O=C)} \rightarrow \pi^*_{(O=C)}]$
$S_0 \rightarrow S_4$	8.24	150	0.007	84.3	H−1 → L	$^1[n \rightarrow \pi^*_{(O=C)}]$
$S_0 \rightarrow S_5$	8.30	149	0.041	40.3	H−2 → L	$^1[\pi_{(O=C)} \rightarrow \pi^*_{(O=C)}]$
				29.0	H−3 → L	
				14.5	H → L+1	$^1[n \rightarrow \sigma^*_{(C-H)}]$

[a] Wavelength.

[b] Oscillator strength.

[c] H and L represent HOMO and LUMO.

[d] Subscripts such as C, O, H, C−H, and O=C represent MOs populated on these atoms and chemical bonds.

Note S1. Conformation Searching

Due to the free rotation of the C−C bond, there are numerous local minima on the potential energy surface (PES) for MPK. To address this issue, the conformation searching plugin Confab[1] integrated into the Open Babel 3.1.1 program[2] is employed to produce the potential conformers of the model compound according to a systematic generation algorithm. After comparing the rough energy using the molecular force field MMFF94[3] among the generated geometries, the candidate conformers for MPK are produced.

After optimizing the candidate MPK conformers using the density functional theory (DFT) method, eight diverse geometries are shown in Figure S1. It should be noted that the chemical composition of MPK is simple, and the number of corresponding rotatable bonds is few. Therefore, the MPK geometry in Figure S1a can be regarded as the one with the lowest total energy, and it is employed as another research model with properties contrasted with the PES landscapes of N-ethylacetamide (NEA) in the ground state (GS) and excited state (ES) for the following quantum chemistry (QC) study.

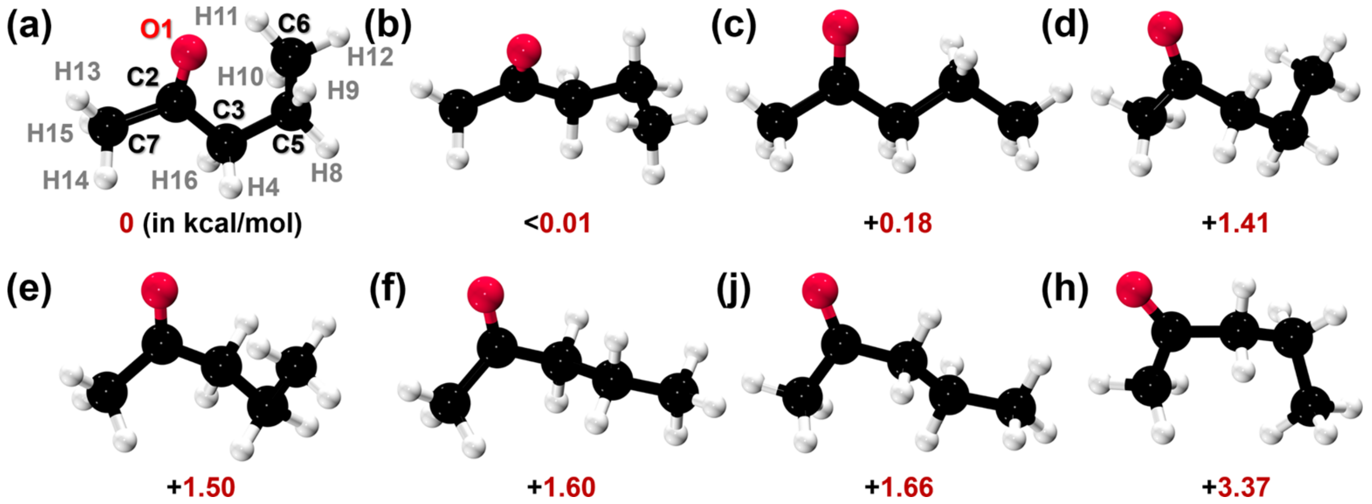

Figure S1. MPK geometries after the PBE0-D3/6-31G(d,p) level optimizations presented in ascending order of relative energy based on conformation screening results. The geometry with the lowest energy was selected for our QC investigations (Figure S1a).

Note S2. Benchmarking on Various (TD-)DFT Methods

To verify the data consistency of the PBE0 functional with other high-level DFT methods, the validation of the default hybrid functional PBE0 in this study was compared with the long range corrected CAM-B3LYP and double-hybrid DSD-PBEP86 DFT methods in the GS and ESs. First, the GS geometry relaxation, $S_0 \rightarrow T_1$, $S_0 \rightarrow S_1$, and $S_0 \rightarrow S_2$ vertical excitation, and molecular orbital (MO) profiles from HOMO−1 to LUMO of NEA were calculated using (TD-)PBE0, (TD-)CAM-B3LYP, and DSD-PBEP86 functionals with the same DFT-D3 and basis set 6-31G(d,p) in Gaussian 16 C.01 software package, the compared main parameters and MOs were shown in Tables S2,3 and Figure S2. Significantly, the vertical excitation work in Table S3, at the TD-DSD-PBEP86-D3/6-31G(d,p) level, was conducted independently at the corresponding GS geometry derived from Gaussian employing ORCA 6.0.1 package.[4-6]

In the density fitting TD-DFT calculation using the double-hybrid functional DSD-PBEP86, the same calculation basis set 6-31G(d,p) was combined with the Becke-Johnson damping scheme DFT-D3 to agree with the GMTKN55 benchmark.[7] However, as no auxiliary basis set was particularly prepared for the Pople basis set, the automatic generation of auxiliary basis[8] was used with this basis set. The method, resolution of the identity approximation to the Coulomb interaction and chain-of-spheres exchange (RIJCOSX),[9] was also utilized for QC acceleration mainly on the hybrid functionals that include an HF component. For this TD-DFT calculation in ORCA, the numerical integration grids were set to the default settings and assigned as 14 (region 1), 26 (region 2), 50 (region 3), 50 (region 4), and 26 (region 5) for the angular grid scheme. As for the radial grid scheme, the grid sizes are 3,467 for the XC and 3,067 for the COSX, respectively. Finally, the energy convergence criterion is 10^{-8} for SCF (‘verytightSCF’).

The doubles (D) correction, proposed by Head-Gordon and co-workers for CIS solutions,[10] is compatible with the philosophy of the double-hybrid functionals and should be used if the excitations are to be computed towards the singlet and triplet ESs. Furthermore, the spin component scaling (SCS) has been incorporated into the functional DSD-PBEP86 in this perturbative CIS(D) part,[11-12] and it was developed and applied to ESs by Schwabe and Goerigk.[13] Therefore, these computation methods should be considered and included in our QC studies. Otherwise, the calculation results would be incorrect. Notably, the four SCS component parameters,[14] i.e., same-spin indirect term, opposite-spin indirect term, same-spin direct term, and opposite-spin direct term, were suggested by Goerigk dedicated for TD-DSD-PBEP86.[15]

In addition, the S_2 state was adopted as the target ES to test the discrepancy of the relaxed ES geometry and corresponding transition nature before and after the $S_0 \rightarrow S_2$ excitation. These terms were compared by the primary structure parameters and leading natural transition orbitals (NTO) for traced ES at the S_2 geometries in Figure S3 and Table S4 between the TD-PBE0-D3/6-31G(d,p) and TD-CAM-B3LYP-D3/6-31G(d,p) levels.

In Table S2, the crucial bond distances, angles, and dihedral angles data of NEA indicate that PBE0-D3/6-31G(d,p) shows a high level of compliance with these structural parameters of CAM-B3LYP-D3/6-31G(d,p). Furthermore, compared with the same data calculated at a more accurate computational level DSD-PBEP86-D3/6-31G(d,p), some crucial bond distance parameters, e.g., the N3−C5 and C2−C7 bond lengths for the CAM-B3LYP-D3 method, show more consistency. In contrast, a good agreement is found within the critical angle and dihedral angle parameters in the PBE0-D3 and DSD-PBEP86-D3 methods.

In Table S3, the excitation energy, absorption peak, oscillator strength, and each dominant transition MOs for the vertical excitation at the individual GS geometry always keep high identical at the TD-PBE0-D3/6-31G(d,p), TD-CAM-B3LYP-D3/6-31G(d,p), and TD-DSD-PBEP86-D3/6-31G(d,p) computational levels, respectively (HOMO → LUMO for $S_0 \rightarrow T_1$, HOMO → LUMO for $S_0 \rightarrow S_1$, and HOMO−1 → LUMO for $S_0 \rightarrow S_2$, leading contribution >60%). For Table S3 and Figure S2, compared with the MOs from HOMO−1 to LUMO of NEA calculated in the default PBE0-D3 method in this investigations, the main transition characteristics for the assignment of $S_0 \rightarrow T_1$, $S_0 \rightarrow S_1$, and $S_0 \rightarrow S_2$ excitations were always designated as $^3[n \rightarrow \pi^*_{(O=C-N)}]$, $^1[n \rightarrow \pi^*_{(O=C-N)}]$, and $^1[n_{Z(O\&N)} \rightarrow \pi^*_{(O=C-N)}]$ using the CAM-B3LYP-D3 approach, which is greatly in line with the results elucidated in Section 3.1. However, the main MO nature in HOMO−1 was assigned as $^1[n_{Z(N)} + \pi_{(O=C)} \rightarrow \pi^*_{(O=C-N)}]$ using the TD-DSD-PBEP86-D3 approach, which is a little different from the HOMO−1 assignment calculated at the PBE0-D3/6-31G(d,p) level.

Finally, after the state tracing optimizations for the significant ES S_2 using the TD-PBE0-D3 and TD-CAM-B3LYP-D3 methods, the leading transition nature and primary structure parameters for the initial S_2 were plotted in Figure S3 and Table S4 after the ES relaxation. In NTO analysis (Figure S3), the transition characteristics for the main assignment of $S_0 \rightarrow S_2$ excitation (>80%) were consistently assigned as $^1[n_{Z(O\&N)} \rightarrow \pi^*_{(O=C-N)}]$ before and after this ES relaxation at either TD-PBE0-D3/6-31G(d,p) or TD-CAM-B3LYP-D3/6-31G(d,p) level, which proves that the transition nature would not make a difference for the two calculational methods in the $S_0 \rightarrow S_2$ excitation, and the ES tracing optimization is successful for these QC calculations. In addition, the primary structure parameters at the S_2 geometry can be reproduced in the computations using the TD-PBE0-D3 and TD-CAM-B3LYP-D3 methods, except for the C2−N3 bond length (Table S4). Although the C2−N3 bond was extended in the same ES using different calculational methods, the C2−N3 bond length is 0.02 Å shorter at the TD-CAM-B3LYP-D3/6-31G(d,p) level (1.44 Å) compared with that at the TD- PBE0-D3/6-31G(d,p) level (1.46 Å). In conclusion, the results mentioned above indicate that the PBE0 hybrid functional is valid and reasonable for our QC studies, as compared and examined with other functionals and high-level methods.

Table S2. Main structure parameter comparison at the GS geometries of NEA using different DFT methods with the same basis set 6-31G(d,p).

	PBE0-D3	**CAM-B3LYP-D3**	**DSD-PBEP86-D3**
Bond distances (Å)			
O1−C2	1.221	1.221	1.228
C2−N3	1.361	1.361	1.366
N3−H4	1.007	1.007	1.007
N3−C5	1.448	1.452	1.455
C2−C7	1.513	1.514	1.517
Angles (°)			
O1−C2−N3	122.48	122.24	122.34
C2−N3−H4	118.95	119.10	118.91
Dihedral angles (°)			
O1−C2−N3−H4	6.83	6.45	8.46
C2−N3−H4−C5	168.68	169.57	166.01

Table S3. Parameter comparison of $S_0 \rightarrow T_1$, $S_0 \rightarrow S_1$, and $S_0 \rightarrow S_2$ vertical excitations (UV absorption) at the GS geometries of NEA (see Table S2) in ascending order of excitation energy using different TD-DFT methods with the same basis set 6-31G(d,p).

Electronic excitation	Energy (eV)	λ (nm)	*f*	Contribution (>10%)	Transitions	Assignments
			TD-PBE0-D3			
$S_0 \rightarrow T_1$	5.15	241	0	84.4	H → L	$^3[n \rightarrow \pi^*_{(O=C-N)}]$
				11.5	H−1 → L	
$S_0 \rightarrow S_1$	5.79	214	0.001	82.6	H → L	$^1[n \rightarrow \pi^*_{(O=C-N)}]$
				16.2	H−1 → L	
$S_0 \rightarrow S_2$	7.47	166	0.150	68.0	H−1 → L	$^1[n \rightarrow \pi^*_{(O=C-N)}]$
				14.2	H → L	
				12.8	H → L+1	$^1[n \rightarrow \sigma^*_{(N-H)}]$
			TD-CAM-B3LYP-D3			
$S_0 \rightarrow T_1$	5.20	238	0	92.5	H → L	$^3[n \rightarrow \pi^*_{(O=C-N)}]$
$S_0 \rightarrow S_1$	5.79	214	0.001	68.1	H → L	$^1[n \rightarrow \pi^*_{(O=C-N)}]$
				29.0	H−1 → L	
$S_0 \rightarrow S_2$	7.62	163	0.162	60.6	H−1 → L	$^1[n \rightarrow \pi^*_{(O=C-N)}]$
				27.6	H → L	
			TD-DSD-PBEP86-D3			
$S_0 \rightarrow T_1$	5.19	239	0	88.7	H → L	$^3[n \rightarrow \pi^*_{(O=C-N)}]$
$S_0 \rightarrow S_1$	5.64	220	0.001	84.5	H → L	$^1[n \rightarrow \pi^*_{(O=C-N)}]$
$S_0 \rightarrow S_2$	7.34	169	0.169	84.4	H−1 → L	$^1[n + \pi_{(O=C)} \rightarrow \pi^*_{(O=C-N)}]$

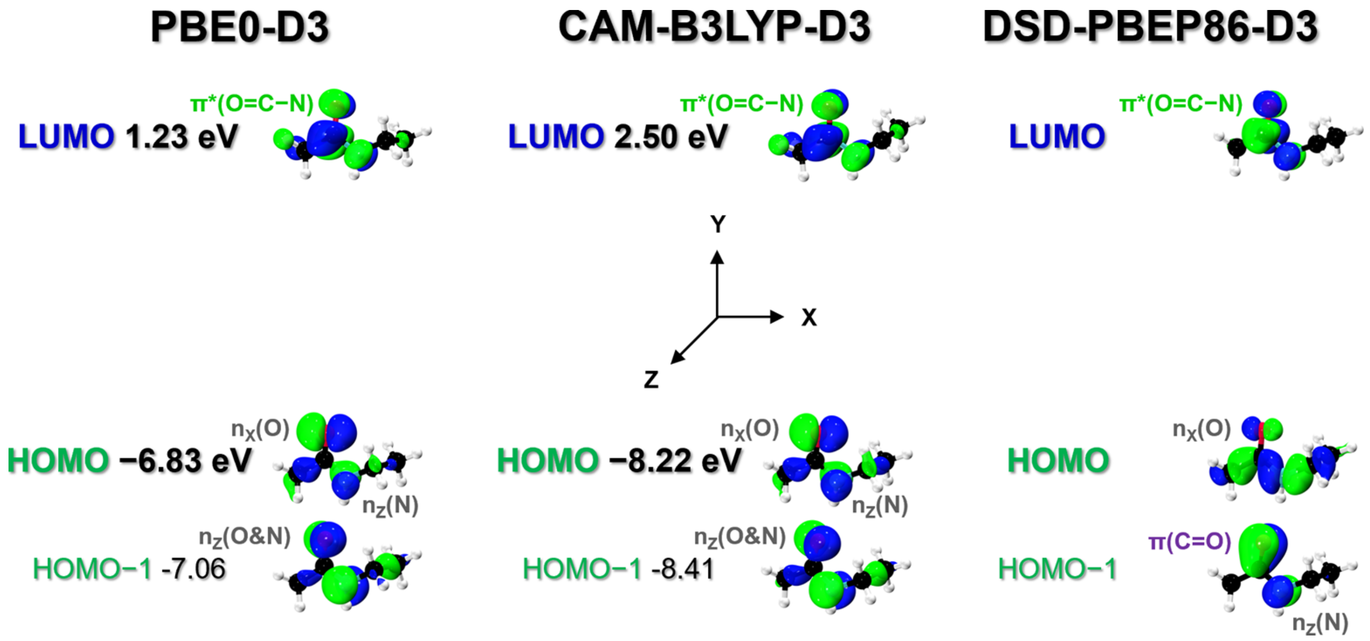

Figure S2. MOs (isovalue = 0.05) from the most concerned HOMO−1 to LUMO for NEA at the respective GS geometries of NEA using hybrid functional PBE0-D3, long-range corrected and double-hybrid functionals (CAM-B3LYP-D3 and DSD-PBEP86-D3, Table S2) with the same basis set 6-31G(d,p).

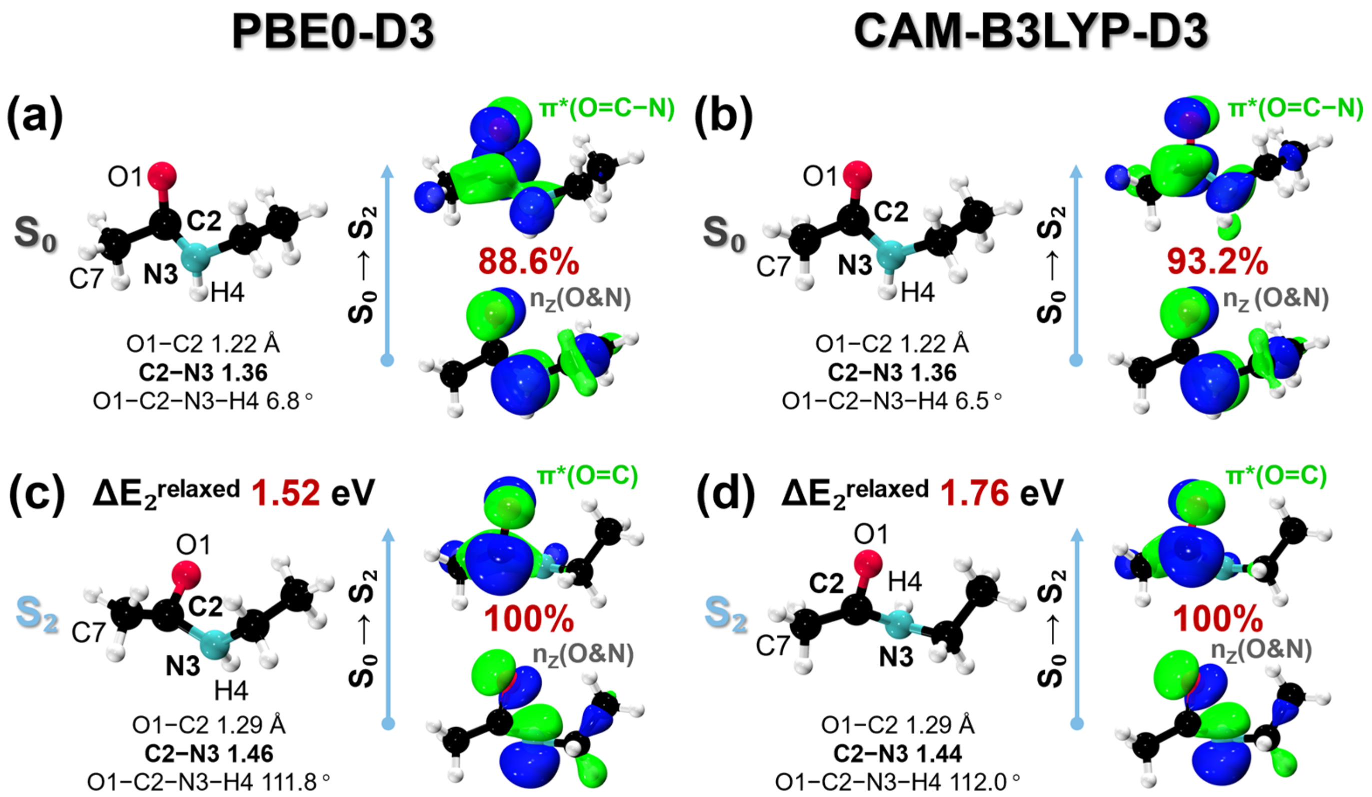

Figure S3. (a) Geometry at the local energy minimum in S_0 for NEA after the (a) PBE0-D3/6-31G(d,p) and (b) CAM-B3LYP-D3/6-31G(d,p) optimization with the critical bond lengths and dihedral angle (in Å and °) and leading NTO (isovalue = 0.05) pairs with the transition nature at the S_0 geometry of NEA (>80%) for the $S_0 \rightarrow S_2$ vertical excitation (blue arrow line). Geometry at the local energy minimum in S_2 for NEA after the (c) TD-PBE0-D3/6-31G(d,p) and (d) TD-CAM-B3LYP-D3/6-31G(d,p) ES optimization with the critical bond lengths and dihedral angle and dominant NTO pair plotted for the $S_0 \rightarrow S_2$ excitation at the S_2 geometry. The corresponding excitation energy after geometry relaxation for S_2 ($\Delta E_2^{relaxed}$) is 1.76 eV (TD-CAM-B3LYP-D3/6-31G(d,p) level).

Table S4. Main structure parameter comparison at the S_2 geometries of NEA using different TD-DFT methods (TD-PBE0-D3 and TD-CAM-B3LYP-D3) with the same basis set 6-31G(d,p).

	TD-PBE0-D3	**TD-CAM-B3LYP-D3**
Bond distances (Å)		
O1−C2	1.290	1.293
C2−N3	1.462	1.442
N3−H4	1.024	1.024
N3−C5	1.439	1.451
C2−C7	1.491	1.491
Angles (°)		
O1−C2−N3	102.63	102.51
C2−N3−H4	115.77	115.72
Dihedral angles (°)		
O1−C2−N3−H4	111.76	111.97
C2−N3−H4−C5	144.72	144.71

Note S3. Complete Active Space Self-Consistent Field Calculation

As the excitation energy from the GS to a specific ES with the same spin multiplicity is extremely low during the adiabatic process for the TD-DFT method, a state-averaged complete active space self-consistent field (SA-CASSCF) calculation was performed to determine whether a conical intersection (CI) exists or not. The active space included eight electrons and eight orbitals (four occupied and four unoccupied) in this CASSCF scheme (Figure S4), which encompasses all the transition molecular orbital (MO) characteristics involved in the ESs for our study on NEA (Figure 2a). The SA-CASSCF calculation over two states coupled with the same basis set, SA2-CAS(8,8)/6-31G(d,p), was performed to obtain the CI correlating with the GS and ES based on the NEA geometries and corresponding wavefunctions at the end of the Norrish reaction, ultimately indicating photodegradation.

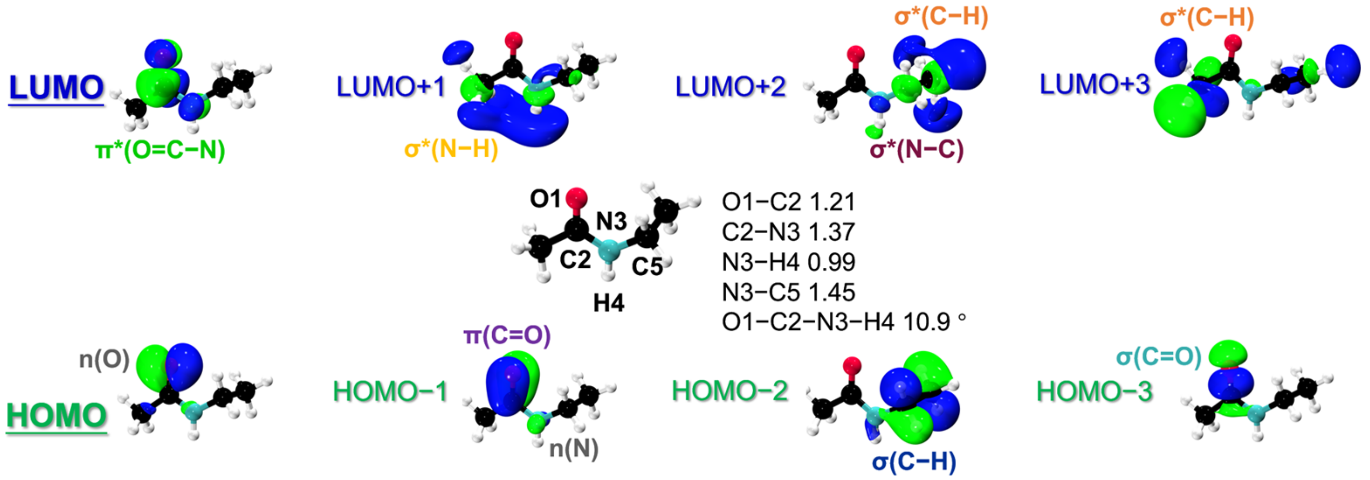

Figure S4. MOs from HOMO−3 to LUMO+3 (isovalue = 0.05) for the optimized NEA geometry in the GS (calculated at the CAS(8,8)/6-31G(d,p) level). The critical structural parameters for bond length (in Å) and dihedral angle (in °) at this geometry are also attached in the plot.

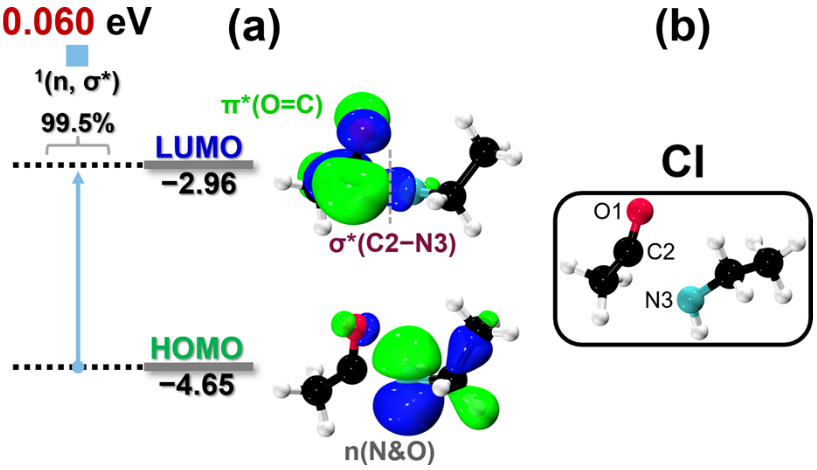

Figure S5. (a) Dominant transition MOs at the $S_{(C2•N3)}$ geometry (Figure 4b) with the transition nature ^{1}[n → $σ^*_{(C2–N3)}$]. The MO contributions (%) and excitation energy (in eV) for this geometry calculated at the TD-DFT level of PBE0-D3/6-31G(d,p) are also included in this figure. (b) Verified CI geometry using SA-CASSCF (SA2-CAS(8,8)/6-31G(d,p) level) correlating with the GS and singlet ES with the same ^{1}(n, σ*) characteristics based on the $S_{(C2•N3)}$ geometry.

130

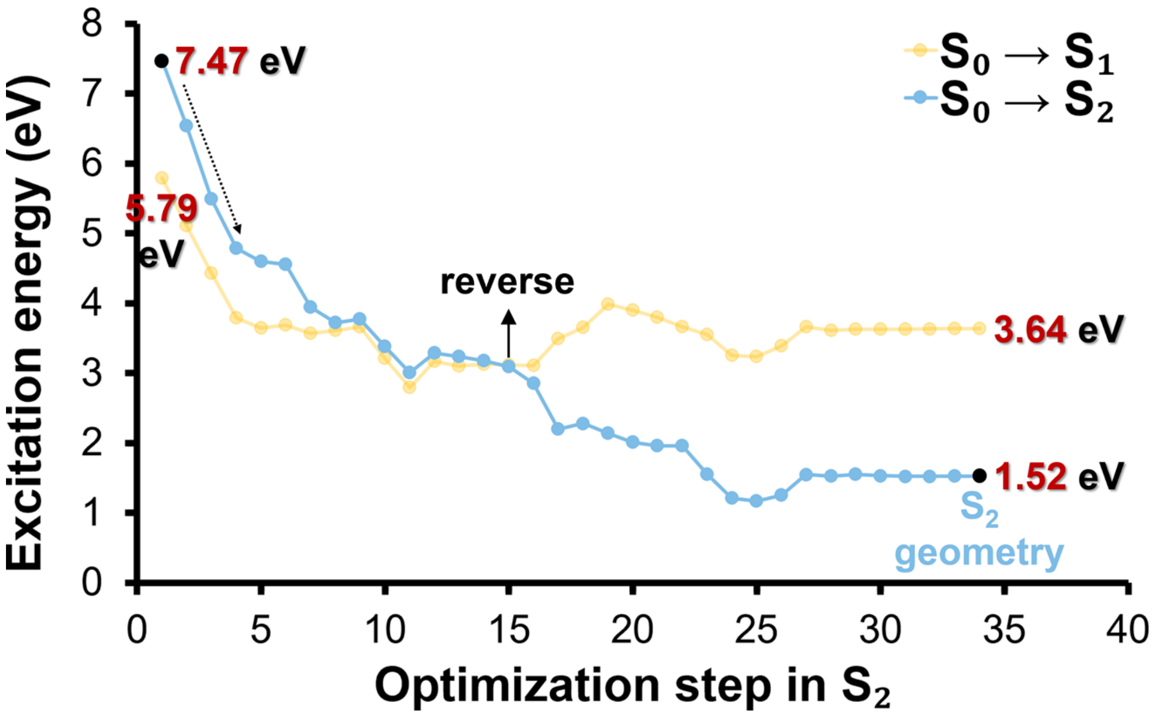

Figure S6. S_1 and S_2 excitation energy variations (in eV) as a function of the S_2 optimization steps for NEA calculated at the TD-PBE0-D3/6-31G(d,p) level.

131

132

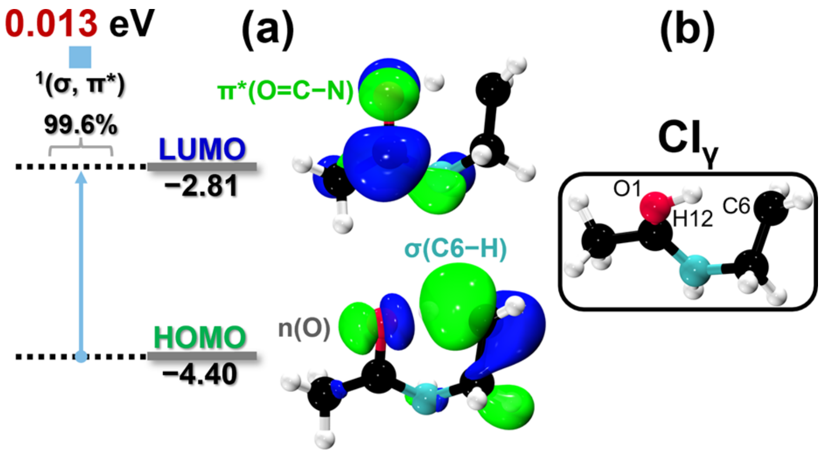

Figure S7. (a) Dominant transition MOs at the $S_{(O\bullet H12)}$ geometry (Figure 6b) with the transition nature $^1[\sigma_{(C6-H12)} \rightarrow \pi^*]$. The MO contributions (%) and excitation energy (in eV) for this geometry calculated at the TD-DFT level of PBE0-D3/6-31G(d,p) are also included in this figure. (b) Verified CI geometry using SA-CASSCF (CI_γ, SA2-CAS(8,8)/6-31G(d,p) level) correlating with the GS and singlet ES with the same $^1(\sigma, \pi^*)$ characteristics based on the $S_{(O\bullet H12)}$ geometry.

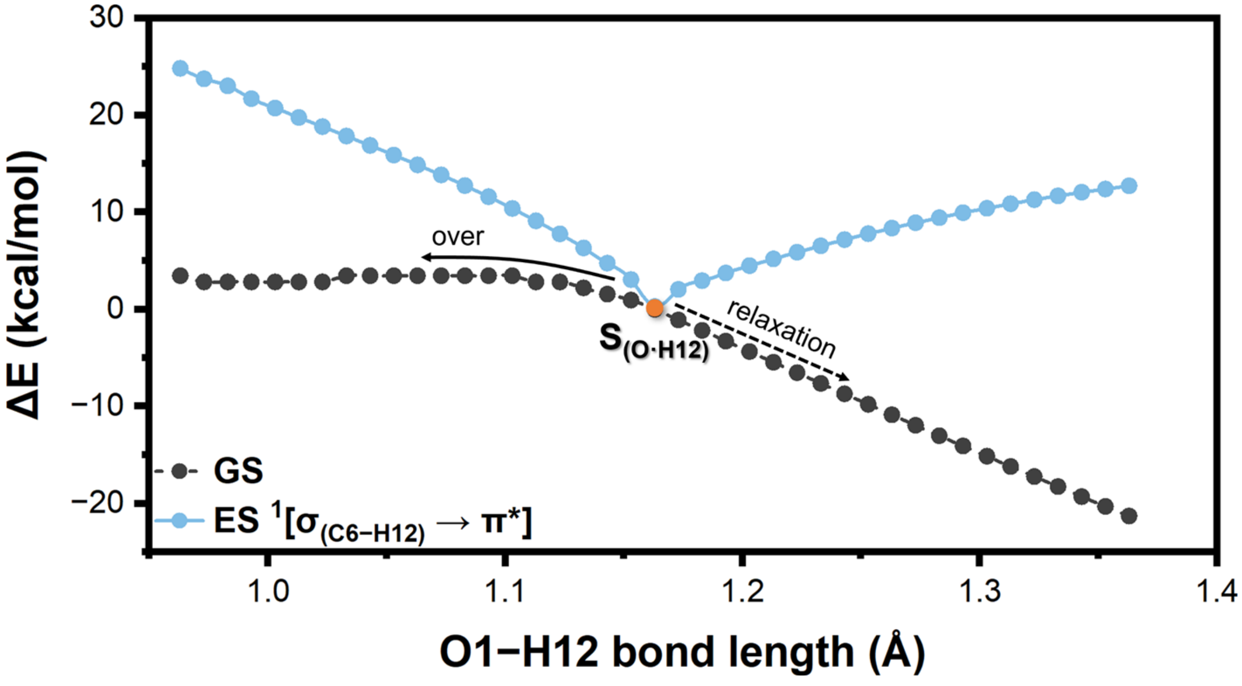

Figure S8. Relative energy curves (ΔE, in kcal/mol) for the PES scan with respect to and based on the $S_{(O\bullet H12)}$ geometry (orange dot, Figures 6b and 7) as a function of the O1−H12 bond length (ranging from 0.96 to 1.36 Å) for the NEA molecule in the GS and singlet ES with the transition nature $^1[\sigma_{(C6-H12)} \rightarrow \pi^*]$ at the (TD-)PBE0-D3/6-31G(d,p) level.

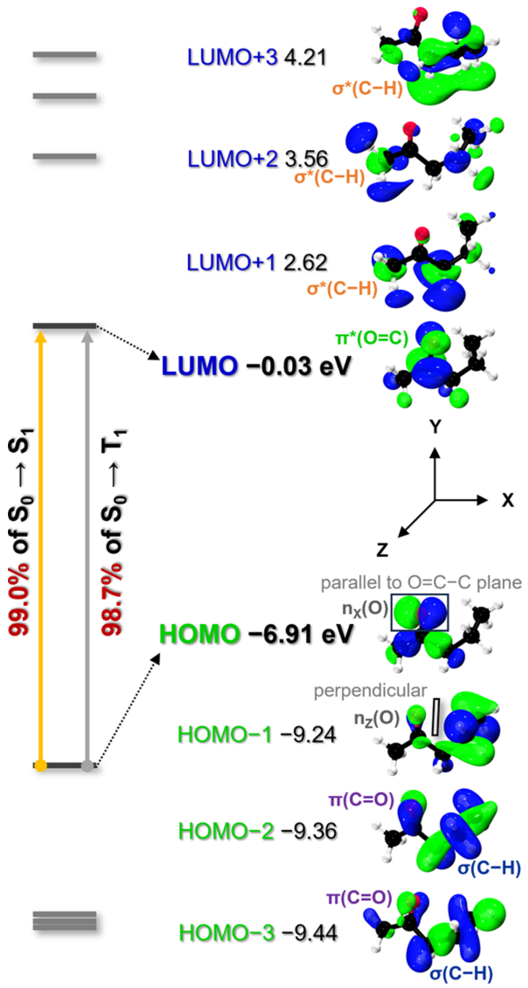

Figure S9. MOs (isovalue = 0.05) from HOMO−3 to LUMO+3 for MPK at the S_0 geometry (PBE0-D3/6-31G(d,p) level, Figures 1b and S1a). The orange and gray arrow lines represent the dominant transition MO assignments (>98%) for the $S_0 \rightarrow S_1$ and $S_0 \rightarrow T_1$ vertical excitations involved in Norrish reaction.

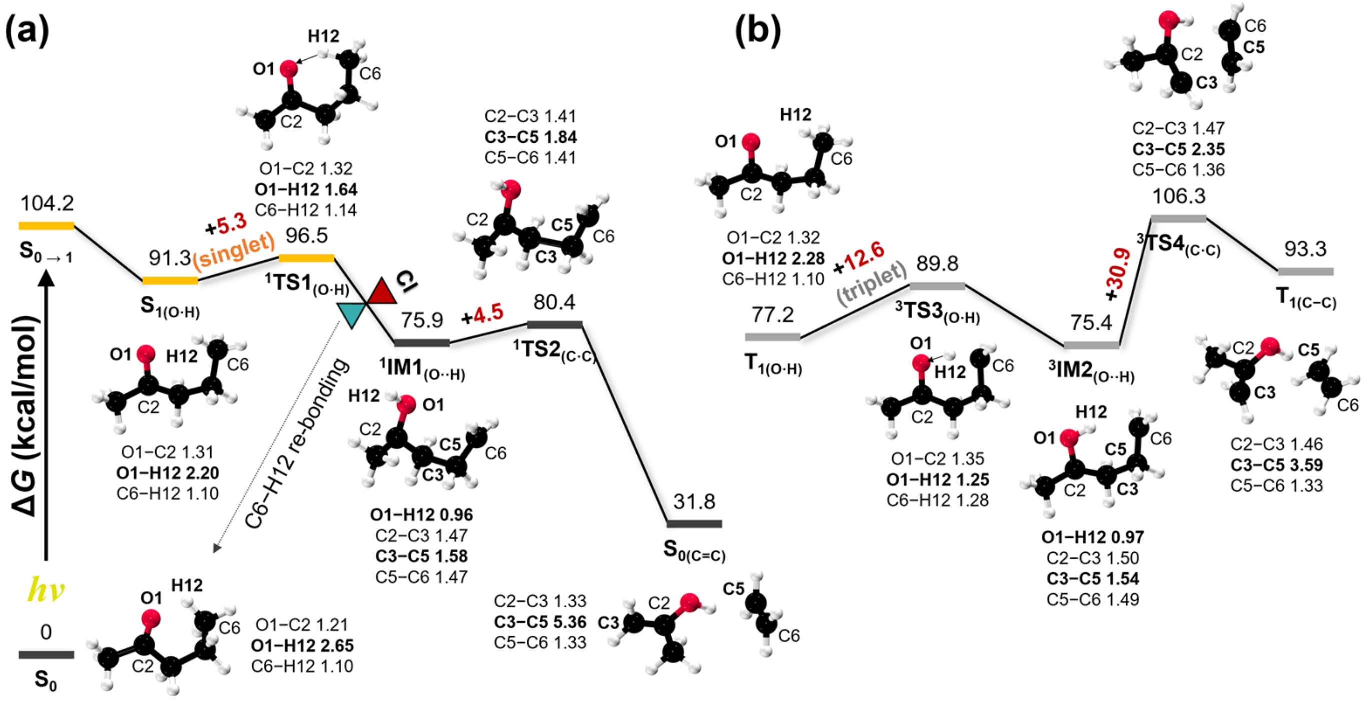

Figure S10. Relative Gibbs free energy (ΔG) profiles (at the (EOM-)CCSD/def2-TZVP level, in kcal/mol) for the MPK Norrish type II reaction in the (a) singlet ES (represented by orange bars), following GS (black bars) and (b) triplet ES (gray bars). In this figure, all MPK geometries are obtained at the (TD-)PBE0-D3/6-31G(d,p) level with the bond length parameters (in Å) for the reactant, TS, intermediate with the O1−H12 bonding, and the product with chain scission. The Norrish type II reaction barrier is also denoted in this figure, and the $S_{1(O•H)}$ or $T_{1(O•H)}$ for MPK is one of the geometries at the local energy minimum in S_1 and T_1.

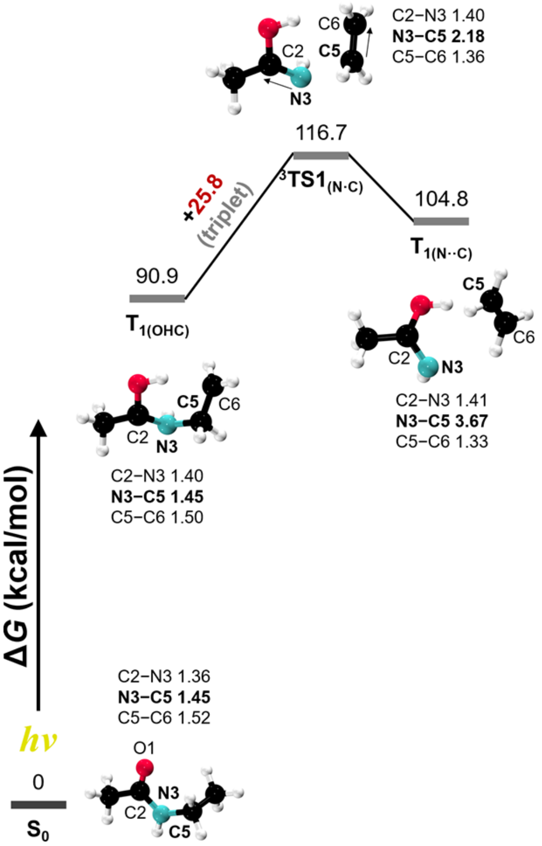

Figure S11. Relative Gibbs free energy (Δ*G*) profiles (at the (EOM-)CCSD/def2-TZVP level, in kcal/mol) for the second reaction step of NEA Norrish type II mechanism in the triplet ES. In this figure, all NEA geometries are obtained at the (TD-)PBE0-D3/6-31G(d,p) level with the bond length parameters (in Å) for the reactant, TS, and the product with chain scission. The reaction barrier is also denoted, and the T$_{1(OHC)}$ geometry in Figure 6c is followed by this figure.

References

1. O'Boyle, N. M.; Vandermeersch, T.; Flynn, C. J.; Maguire, A. R.; Hutchison, G. R. Confab-Systematic Generation of Diverse Low-Energy Conformers. *J. Cheminf.* **2011**, *3* (1), 8. DOI: 10.1186/1758-2946-3-8

2. O'Boyle, N. M.; Banck, M.; James, C. A.; Morley, C.; Vandermeersch, T.; Hutchison, G. R. Open Babel: An Open Chemical Toolbox. *J. Cheminf.* **2011**, *3* (1), 33. DOI: 10.1186/1758-2946-3-33

3. Halgren, T. A. Merck Molecular Force Field. III. Molecular Geometries and Vibrational Frequencies for MMFF94. *J. Comput. Chem.* **1996**, *17* (5–6), 553–586. DOI: 10.1002/(SICI)1096-987X(199604)17:5/6<553::AID-JCC3>3.0.CO;2-T

4. Neese, F. The ORCA Program System. *WIRES Comput. Molec. Sci.* **2012**, *2* (1), 73–78. DOI: 10.1002/wcms.81

5. Neese, F.; Wennmohs, F.; Becker, U.; Riplinger, C. The ORCA Quantum Chemistry Program Package. *J. Chem. Phys.* **2020**, *152* (22), 224108. DOI: 10.1063/5.0004608

6. Neese, F. Software Update: the ORCA Program System—Version 5.0. *WIRES Comput. Molec. Sci.* **2022**, *12* (1), e1606. DOI: 10.1002/wcms.1606

7. Goerigk, L.; Hansen, A.; Bauer, C.; Ehrlich, S.; Najibi, A.; Grimme, S. A Look at the Density Functional Theory Zoo with the Advanced GMTKN55 Database for General Main Group Thermochemistry, Kinetics and Noncovalent Interactions. *Phys. Chem. Chem. Phys.* **2017**, *19* (48), 32184–32215. DOI: 10.1039/C7CP04913G

8. Stoychev, G. L.; Auer, A. A.; Neese, F. Automatic Generation of Auxiliary Basis Sets. *J. Chem. Theory Comput.* **2017**, *13* (2), 554–562. DOI: 10.1021/acs.jctc.6b01041

9. Neese, F.; Wennmohs, F.; Hansen, A.; Becker, U. Efficient, Approximate and Parallel Hartree–Fock and Hybrid DFT Calculations. A "Chain-of-Spheres" Algorithm for the Hartree–Fock Exchange. *Chem. Phys.* **2009**, *356* (1–3), 98–109. DOI:

10.1016/j.chemphys.2008.10.036

10. Head-Gordon, M.; Rico, R. J.; Oumi, M.; Lee, T. J. A Doubles Correction to Electronic Excited States from Configuration Interaction in the Space of Single Substitutions. *Chem. Phys. Lett.* **1994**, *219* (1–2), 21–29. DOI: 10.1016/0009-2614(94)00070-0

11. Kozuch, S.; Martin, J. M. L. DSD-PBEP86: in Search of the Best Double-Hybrid DFT with Spin-Component Scaled MP2 and Dispersion Corrections. *Phys. Chem. Chem. Phys.* **2011**, *13* (45), 20104. DOI: 10.1039/C1CP22592H

12. Kozuch, S.; Martin, J. M. L. Spin-Component-Scaled Double Hybrids: An Extensive Search for the Best Fifth-Rung Functionals Blending DFT and Perturbation Theory. *J. Comput. Chem.* **2013**, *34* (27), 2327−2344. DOI: 10.1002/jcc.23391

13. Schwabe, T.; Goerigk, L. Time-Dependent Double-Hybrid Density Functionals with Spin-Component and Spin-Opposite Scaling. *J. Chem. Theory Comput.* **2017**, *13* (9), 4307–4323. DOI: 10.1021/acs.jctc.7b00386

14. Rhee, Y. M.; Head-Gordon, M. Scaled Second-Order Perturbation Corrections to Configuration Interaction Singles: Efficient and Reliable Excitation Energy Methods. *J. Phys. Chem. A* **2007**, *111* (24), 5314–5326. DOI: 10.1021/jp068409j

15. Sebastian, S.; Riley, V.; Wanniarachchi, B.; Ritchie, C.; Goerigk, L. Spin-Scaled Double Hybrids with Long-Range Correction Solve the TD-DFT Overestimation Problem in BODIPY Dyes: Benchmarking and Experimental Validation. https://doi.org/10.26434/chemrxiv-2025-1mqbt-v3